Convective generation and vertical propagation of fast gravity waves on Mars: One- and two-dimensional modeling

Takeshi Imamura [a,*], Ayuka Watanabe [b], Yasumitsu Maejima [c]

[a] Institute of Space and Astronautical Science, Japan Aerospace Exploration Agency, 3-1-1, Yoshinodai, Chuo-ku, Sagamihara, Kanagawa 252-5210, Japan
[b] Department of Earth and Planetary Science, The University of Tokyo, 7-3-1 Hongo, Bunkyo-ku, Tokyo 113-0033, Japan
[c] RIKEN Advanced Institute for Computational Science, 7-1-26, Minatojima-minami-machi, Chuo-ku, Kobe, Hyogo 650-0047, Japan

A B S T R A C T

Generation of gravity waves by convection was studied using a nonlinear two-dimensional model. A boundary-layer convection forced by a horizontally-uniform heating and a plume forced by a localized heating representing a local dust storm were tested. The results suggest that vigorous convection occurs due to the low density of the martian atmosphere and that short-period waves having frequencies near the buoyancy frequency can be preferentially generated. The propagation of those gravity waves to thermospheric heights was studied using a linearized one-dimensional model. Because of the fast vertical propagation the waves attain large amplitudes in the lower thermosphere, being consistent with Mars Global Surveyor and Mars Odyssey's accelerometer measurements and MAVEN's neutral and ion measurements. The heating and cooling caused by the waves are expected to be significant in the energy budget of the thermosphere, and the vertical mixing induced by those gravity waves should influence the homopause height. Since the thermospheric densities of light, minor species increase with the lowering of the homopause, a lower homopause may have enhanced the escape of such species to space for early Mars, where slower, weaker gravity waves should dominate.

© 2015 Elsevier Inc. All rights reserved.

1. Introduction

Gravity waves are thought to be ubiquitous in the martian atmosphere similarly to the Earth's atmosphere. Observations by entry probes (Magalhães et al., 1999) and radio occultation measurements (Hinson et al., 1999; Creasey et al., 2006a) showed short-vertical scale (<10 km) fluctuations in temperature, which are indicative of gravity waves. The laser altimeter on Mars Global Surveyor (MGS) observed echoes from cloud tops in the northern polar latitude, and showed that sloping wavefronts with horizontal wavelengths of several tens of kilometers are commonly observed (Pettengill and Ford, 2000). Horizontal wavenumber spectra of the atmospheric temperature taken by MGS at wavelengths of 60–1000 km suggest a major contribution of gravity waves (Imamura et al., 2007). Accelerometer data taken during the aerobraking of MGS and Mars Odyssey (Withers, 2006; Creasey et al., 2006b; Fritts et al., 2006) showed wavelike density fluctuations of 5–50% with horizontal scales of 20–200 km in the lower thermosphere (100–130 km). Wavelike features are also observed in the airglow images taken by OMEGA onboard Mars Express on horizontal

scales of 50–150 km (Altieri et al., 2012). Recently the neutral and ion measurements on NASA's MAVEN spacecraft detected wavelike features with similar scales in the densities of neutral and ion species in the lower thermosphere (Mahaffy et al., 2015).

Fritts et al. (2006) suggested that amplitudes of topographically-generated gravity waves in the martian atmosphere might be larger than their terrestrial analogs on the grounds that the topography on Mars at small scales is large and the strong winter zonal jets extend down to low altitudes. Joshi et al. (1995) parameterized such topographically-generated waves and applied the parameterization to martian general circulation models (GCMs). Spiga et al. (2012) employed a three-dimensional mesoscale model to simulate excitation of gravity waves by flows impinging on a mountain, and showed that waves with horizontal wavelengths of ~100 km propagate to the lower thermosphere and cause large temperature fluctuations, which locally force CO_2 to condense.

Topography is not the only source of gravity waves: convection, shear instability near strong jets, and wave–wave interactions are also expected to be operative. Creasey et al. (2006a) analyzed MGS radio science data and found significant wave activity over the tropics and little correlation of the wave potential energy with underlying topography, suggesting that wave sources other than

* Corresponding author.
  E-mail address: imamura.takeshi@jaxa.jp (T. Imamura).

topography play an important role. Wright (2012) analyzed the temperature measurements by Mars Climate Sounder on Mars Reconnaissance Orbiter and showed that there appears to be minimal association between wave activity and topography. These results suggest a possible major contribution of convection in wave generation, although filtering of waves in the upper atmosphere may obscure the influence of the geographical distribution of wave sources. The existence of a convective boundary layer extending to heights of 3–10 km has been suggested by radio occultation observations of the temperature profile (Hinson et al., 2008). Given the expected strong convection in the tenuous atmosphere of Mars (Odaka et al., 1998; Michaels and Rafkin, 2004), wave generation by convection on Mars can be more intense than terrestrial analogues. In the Earth's atmosphere, localized convective storms are considered as important wave sources (Fovell et al., 1992; Walterscheid et al., 2001; Horinouchi et al., 2002) as well as dry convection in the boundary layer (Goya and Miyahara, 1999; Lane and Clark, 2002). Qualitatively similar, localized convective systems can exist on Mars: local dust storms develop when convective energy is supplied by the absorption of incoming sunlight by suspended dust particles, rather than by latent heating as in moist convection on the Earth (Spiga et al., 2013). On the other hand, the absence of notable correlation of thermospheric wave activity with the local time (Fritts et al., 2006) might suggest a limited contribution of convectively-generated waves. However, detached neutral stability layers are widely observed on the nightside by radio occultation, and they are attributed to convection driven by radiative cooling associated with the formation of water ice clouds (Hinson et al., 2014); wave generation by such nocturnal convection might diminish the local time dependence. Medvedev et al. (2011a, 2011b) assumed, in their Mars GCMs, a Gaussian-shaped phase velocity spectrum of gravity waves centered at the mean wind velocity at the source level, and suggested strong influence of gravity waves on the planetary-scale wind distribution. The occurrence of both positive and negative phase velocities is typical of gravity waves generated by convection. We should note, however, that the typical phase velocity and period are poorly constrained. No effort has been made in previous works to simulate convective generation of gravity waves on Mars, although convective generation is one of the basic wave generation processes.

Gravity waves are expected to induce vertical mixing in the martian upper atmosphere by driving planetary-scale meridional circulation via momentum deposition and by generating turbulence (Barnes, 1990; Théodore et al., 1993; Joshi et al., 1995; Kuroda et al., 2009; Medvedev et al., 2011a, 2011b). The occurrence of wave breaking in the martian middle atmosphere has been suggested from temperature profiles (Heavens et al., 2010; Ando et al., 2012). Parish et al. (2009) calculated using a linear model the vertical structures of gravity waves similar to those observed in the polar region, and predicted that the waves propagate to heights of ∼200 km. The vertical mixing induced by such high-altitude waves should play a crucial role in the control of the homopause, which separates the homosphere and the heterosphere (Yamanaka, 1995). In the homosphere gases are well mixed by fluid motions, while in the heterosphere molecular diffusion dominates and each species tends to be distributed with its individual scale height. The location of the homopause influences the thermospheric composition and thereby the species escaping to space. On Earth the homopause is typically located near 105 km altitude (100 nbar), while on Mars it lies near 125 km (1 nbar) (Mueller-Wodarg et al., 2008); the relatively low pressure at the martian homopause implies a fast vertical mixing.

Thermal effects of gravity waves can also be significant in the martian upper atmosphere. Parish et al. (2009) and Walterscheid et al. (2013) suggested, based on one-dimensional modeling, that gravity waves induce heating around 120–150 km and cooling

above due to an irreversible conversion of mechanical wave energy into heat and differential heating/cooling due to the divergence of the induced downward sensible heat flux. Medvedev and Yiğit (2012) incorporated the wave-induced heating and cooling into a martian GCM and showed that the effects can be comparable with radiative effects. Medvedev et al. (2015) argued that the wave-induced cooling of the thermosphere might explain the discrepancy between the observed and model-derived temperatures.

Although the crucial importance of martian gravity waves has been widely recognized, the excitation mechanisms and the factors controlling the wave parameters are left unsolved. In this paper we employ numerical models to study the characteristics of martian gravity waves originating from convection. Two types of convection are considered: boundary-layer convection driven by a horizontally-uniform heating near the surface, and a plume driven by a localized heating representing a local dust storm. We simulate the generation of gravity waves from convection using a nonlinear local model, and study the propagation characteristics of the waves in the upper atmosphere using a linear model. The current study is restricted to a two-dimensional atmosphere with no background wind; it is considered a simplifying first step in understanding complicated three-dimensional interactions between convection and overlying atmosphere. The remainder of this paper is as follows: Section 2 describes the configuration of the nonlinear convection model, Section 3 shows the model results of wave generation, Section 4 obtains linear solutions of vertically-propagating waves, and the summary and conclusions are given in Section 5.

2. Description of the nonlinear convection model

2.1. Fluid dynamical model

A two-dimensional, nonlinear, local model of the martian atmosphere was developed using CReSS (Cloud Resolving Storm Simulator) version 2.3, which is described by Tsuboki and Sakakibara (2002, 2007) in detail. The overall structure of the model is similar to that of the Venus' two-dimensional convection model by Imamura et al. (2014). The dependent variables are horizontal velocity u, vertical velocity w, perturbation potential temperature θ', and perturbation pressure p'. The governing equations are:

$$\frac{\partial \bar{\rho} u}{\partial t} = -\bar{\rho}\left(u\frac{\partial u}{\partial x} + w\frac{\partial u}{\partial z}\right) - \frac{\partial p'}{\partial x} + Turb.u, \tag{1}$$

$$\frac{\partial \bar{\rho} w}{\partial t} = -\bar{\rho}\left(u\frac{\partial w}{\partial x} + w\frac{\partial w}{\partial z}\right) - \frac{\partial p'}{\partial z} + \bar{\rho}g\left(\frac{\theta'}{\bar{\theta}} - \frac{p'}{\bar{\rho}c_S^2}\right) + Turb.w, \tag{2}$$

$$\frac{\partial \bar{\rho} \theta'}{\partial t} = -\bar{\rho}\left(u\frac{\partial \theta'}{\partial x} + w\frac{\partial \theta'}{\partial z}\right) - \bar{\rho}w\frac{\partial \bar{\theta}}{\partial z} + \bar{\rho}\frac{d\theta}{dt} + Turb.\theta, \tag{3}$$

$$\frac{\partial p'}{\partial t} = -\left(u\frac{\partial p'}{\partial x} + w\frac{\partial p'}{\partial z}\right) + \bar{\rho}gw - \bar{\rho}c_S^2\left(\frac{\partial u}{\partial x} + \frac{\partial w}{\partial z}\right) + \frac{\bar{\rho}c_S^2}{\theta}\frac{d\theta}{dt}, \tag{4}$$

where x and z are the horizontal and vertical coordinate, respectively, t is the time, $\bar{\rho}$ and $\bar{\theta}$ are the basic-state density and potential temperature, respectively, g is the gravitational acceleration, c_s is the sound speed, and θ is the total potential temperature. The diabatic heating $d\theta/dt$ is given by prescribed forcing functions: 'uniform heating' for simulating a boundary-layer convection (Section 2.2) and 'localized heating' for simulating a plume representing a local dust storm (Section 2.3). A list of the model runs is given in Table 1. $Turb.u$, $Turb.w$ and $Turb.\theta$ represent subgrid-scale diffusion terms. The eddy diffusion coefficient used in these diffusion terms is taken to be proportional to the 1.5th order turbulence kinetic energy, which develops according to a prognostic equation (Klemp and Wilhelmson, 1978). Radiative damping is not included

Table 1
List of convection model runs.

Heating configuration	Sensitivity test	Specification of heating
Uniform heating model	UNI-ST	40 K h^{-1} in the bottom layer (Standard)
	UNI-10%	4 K h^{-1} in the bottom layer
	UNI-1%	0.4 K h^{-1} in the bottom layer
Localized heating model	LOC-ST	20 K h^{-1} at the peak, 60 km span (Standard)
	LOC-10%	2 K h^{-1} at the peak, 60 km span
	LOC-30 km	20 K h^{-1} at the peak, 30 km span

because its effect is small for waves studied in this paper (Section 4).

The physical domain spans altitudes from 0 to 100 km, above which a 50 km-depth Rayleigh damping layer exists to suppress wave reflection. The horizontal domain width is 300 km. Rigid-wall boundary condition is applied to the top and bottom boundaries, while periodic boundary condition and radiational boundary condition are applied to the side boundaries in the uniform heating model and the local heating model, respectively. Rotational effects are neglected since we focus on mesoscale processes in which the Coriolis and other metric terms are unimportant. The specific heat at constant pressure is 860 J kg^{-1} K^{-1} and the gas constant is 192 J kg^{-1} K^{-1} (Zurek, 1992).

The vertical and horizontal grid widths are 0.25 km and 0.5 km, respectively. It was confirmed that a test run with grid widths larger by a factor of 2 does not change the result significantly. The Arakawa-C and Lorenz staggered grids are used for horizontal and vertical grid arrangement, respectively. Effects of sound waves are weakened by adding reduction factors for divergence terms. To further suppress numerical instability, fourth-order numerical smoothing of the dependent variables is applied. It was confirmed in another test run not described here that gravity waves that are consistent with the dispersion relation are reproduced when monochromatic waves are forced at the bottom boundary.

The initial temperature T_0 is given by an analytical expression in unit of Kelvins (Fig. 1):

$$T_0(z) = 180 + 50 \ \tanh\left(\frac{z - 125}{15}\right) + 70 \ \exp\left(-\frac{z}{40}\right)$$
$$\text{for } z > 5 \text{ km}, \tag{5}$$
$$T_0(z) = 213.40 - 4.33z \quad \text{for } z < 5 \text{ km}, \tag{6}$$

where z is the altitude in unit of kilometers. This temperature profile resembles those used in the computation of radiative damping rates by Eckermann et al. (2011), who defined the profiles based on the mean profile at 40°N from the Mars Climate Database (Lewis et al., 1999) for average levels of dust loading and moderate solar activity. In the lowest 5 km the lapse rate is set equal to the adiabatic lapse rate of 4.33 K km^{-1} based on the radio occultation results that the convective boundary layer extends to heights of 3–10 km above the surface (Hinson et al., 2008). The surface pressure is taken to be 6 hPa, and the pressure profile satisfies hydrostatic equilibrium. The initial wind velocity is taken to be zero.

There are two mechanisms through which convective eddies generate gravity waves in an overlying layer (e.g., Fovell et al., 1992). The first one is "mechanical oscillator effect", in which oscillating updrafts and downdrafts impinging on the interface between the unstable and stable regions cause oscillating displacements of the isentropes, thereby exciting gravity waves. The second is "obstacle effect" or "quasi-stationary forcing", in which the perturbed pressure field produced by convection acts as an obstruction to the environmental horizontal flow, thereby generat-
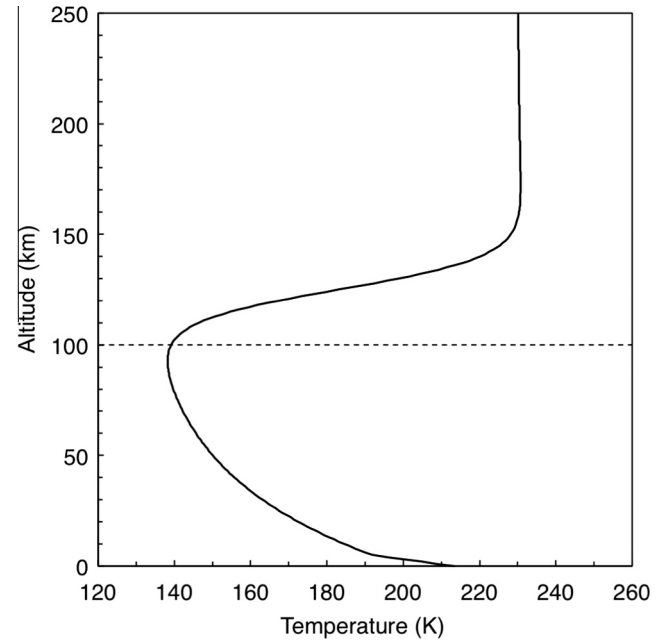

Fig. 1. Background temperature profile used both in the nonlinear convection model and the linear wave model. The top of the physical domain in the nonlinear convection model is 100 km and is indicated by the dashed line. In the linear wave model the asymptotic temperature of 230 K extends to 500 km altitude.

ing waves. The present study, given the absence of background winds, does not allow the latter mechanism to work.

2.2. Uniform heating

In the uniform heating model that represents a boundary-layer convection, a steady heating rate is given in the lowest grid with 0.25 km thickness. The heating rate is chosen so that the energy lost from the boundary layer through radiative cooling during night is replenished by the heating of the bottom layer. Haberle et al. (1993) developed a one-dimensional boundary layer model, which reproduces the basic meteorological properties observed by Viking landers, and estimated the radiative cooling rate of $\sim$50 K day^{-1} in the boundary layer. Assuming the boundary-layer thickness of $\sim$5 km (Hinson et al., 2008), the heating rate in the lowest grid is given by (50 K day^{-1}) × (5 km)/(0.25 km) $\sim$ 42 K h^{-1}. Based on this estimate, the heating rate of 40 K h^{-1} is given in the lowest grid in the standard heating case (UNI-ST). This heating rate corresponds to the vertically-integrated energy supply of 37 W m^{-2}, which is 6% of the solar constant at the martian orbit of 590 W m^{-2}. In the regional model by Odaka et al. (1998), convection was forced by a homogeneous cooling of 50 K day^{-1} in the layer below 5 km altitude; the forcing strength in our model is similar to that of Odaka et al. (1998). In addition to this standard heating, we also conduct a test run with a heating rate of 4 K h^{-1} which is 10% of the standard value (UNI-10%), and a test run with a heating rate of 0.4 K h^{-1} which is 1% of the standard value (UNI-1%).

2.3. Localized heating

In the localized heating model, we consider a situation where a dust cloud with a horizontal scale of several tens of kilometers is heated by solar radiation. Spiga et al. (2013) used a regional model that includes the transport of radiatively active dust to simulate the evolution of a local dust storm. They assumed two types of dust perturbation: a dust cloud with a horizontal span of $\sim$60 km and a

depth of 10 km in the initial state, and a dust lifting through near-surface winds over the same area starting from no initial dust perturbation (Fig. 12 in their paper). In both cases the evolution of the dust storm is governed by deep convective motions.

The modeling by Spiga et al. (2013) shows that updrafts within the dust storm reach $\sim$10 m s^{-1}, and that the radiative heating rate in the dust plume reaches 24 K h^{-1}. The dust that was distributed near the surface in the initial state is removed upward within 1–2 h. Since our model does not include the transport of radiatively active dust, we focus on the diabatic heating that occurs at the initial stage of dust lifting by placing a bubble-shaped heating region adjacent to the surface at the center of the horizontal domain. Then, in the standard heating case (LOC-ST), the spatial distribution and the temporal development of the heating rate q are represented by half cosine curves:

$$q = q_{max} \cos \frac{\pi(x - x_{center})}{x_{width}} \cos \frac{\pi(z - z_{center})}{z_{width}} \cos \frac{\pi(t - t_{center})}{t_{width}}$$

$$\text{for } |x - x_{center}| < \frac{x_{width}}{2}, \quad |z - z_{center}| < \frac{z_{width}}{2}, |t - t_{center}| < \frac{t_{width}}{2},$$

$$q = 0 \quad \text{for other } x, z \text{ and } t, \tag{7}$$

where q_{max} = 20 K h^{-1} is the peak heating rate given according to Spiga et al. (2013), x_{center} = 150 km is the horizontal position where the heating peaks, x_{width} = 60 km is the horizontal span of the heating, z_{center} = 1.5 km is the peak height of the heating, z_{width} = 3 km is the depth of the heating, t_{center} = 1 h is the time when the heating peaks, and t_{width} = 2 h is the duration of the heating. Though the vertical extent of the heating, 0–3 km above the surface, is rather arbitrary, this is considered as a transient state that commonly occurs in the initial phase of dust lifting. The vertically-integrated heating at $x = x_{center}$ and $t = t_{center}$ is $\sim$126 W m^{-2}, which is 20% of the solar constant at the martian orbit. In addition to this standard heating, we conduct a test run with a peak heating rate of q_{max} = 2 K h^{-1} which is 10% of the standard value (LOC-10%), and a test run with a horizontal span of the heating of x_{width} = 30 km which is half of the standard value (LOC-30 km).

It should be noted that the amplitudes of gravity waves generated by a localized forcing in the two-dimensional model are overestimated as compared to those in the three-dimensional atmosphere. The ratio of the amplitude in two-dimension to that in three-dimension is evaluated similarly to the ratio of the electric field of an infinite line charge to that of a point charge with the same charge density. Letting the charge density be q, the vertical thickness of the charge be D, the horizontal span of the charge be L, and the permittivity of vacuum be ε_0, the electric field at the distance R from this localized "point" charge is given by $qDL^2/4\pi\varepsilon_0 R^2$. For a line charge having the same charge density, the same vertical thickness, and the horizontal width L, the electric field is given by $qDL/2\pi\varepsilon_0 R$. Then the ratio is given by $2R/L$, where R and L are regarded as the distance to the convective plume and the horizontal span of the plume, respectively, in this study. For example, considering waves propagating at an elevation angle of $\sim$45° and reaching 60 km height, R is $\sim$100 km. Then, given $L \sim$ 60 km, the ratio is 3.3; the calculated amplitude is considered to be overestimated by this factor.

3. Characteristics of convection and wave generation

3.1. Uniform heating

In the standard case (UNI-ST) the strength of convection and the amplitudes of gravity waves reach quasi-steady states in $\sim$200 min, while in weaker forcing cases (UNI-10% and UNI-1%) they reach quasi-steady states in $\sim$360 min. The dominant wave

modes studied later reach 100 km altitude in one hour after excitation. Fig. 2 shows a close-up of the vertical velocity and temperature perturbation fields near the surface at 200 min in UNI-ST. The thermal forcing drives convection below $\sim$8 km, and the penetration of narrow, hot plumes into the overlying stable layer generates gravity waves. The tilted wavefronts above 10 km altitude principally move downward. The root-mean-square vertical velocity in the convective layer is $\sim$10 m s^{-1} similarly to the result of the two-dimensional model by Odaka et al. (1998). The convective heat flux peaks just above the heated bottom layer with a peak value which is about 90% of the energy supply in the bottom layer; the residual is used for heating the atmosphere near the bottom.

Fig. 3 shows the vertical velocity and the perturbation temperature fields in the whole physical domain at 200 min. The tilted phase surfaces propagate principally downward, and the angle of inclination is typically 30–45°, suggesting that the horizontal and vertical wavenumbers are similar in magnitude. Such gravity waves should have periods comparable to the buoyancy period according to the dispersion relation. Dominance of waves with horizontal and vertical wavelengths of tens of kilometers is evident. The amplitudes of the gravity waves grow with height and induce convective overturning above $\sim$40 km. The peak values of the vertical velocity exceed 30 m s^{-1} in the upper part of the model domain.

To identify the dominant wave modes excited, spectral analysis is employed. Fig. 4 shows the two-dimensional power spectra of the vertical velocity in quasi-steady states: the vertical velocity is suitable for the measure of gravity wave activity. Fig. 4a–c shows the spectra at 60 km, 15 km and 5 km altitudes, respectively, in the standard forcing case (UNI-ST). Since the model is isotropic in horizontal direction, the positive and negative wavenumber components were averaged. The unit of the spectral density is m^2 s^{-2}/log$_2$(wavenumber)/log$_2$(frequency), i.e. the squared amplitude in each power of two of the wavenumber and the frequency. Here we take the square root of this quantity as the amplitude for each wavenumber and frequency.

The maximum power occurs at wavenumbers 0.02–0.1 km^{-1} (wavelengths of 10–50 km) all through the altitude, reflecting the spatial scale of convection cells, and a non-negligible power extends to a wavenumber of $\sim$0.01 km^{-1} (wavelength $\sim$ 100 km). In the convective boundary layer (Fig. 4c) the frequency spectrum is red: the power peaks at the lowest frequency of 1.3×10^{-4} Hz (period $\sim$ 2 h) and decreases with frequency. Just above the convective layer (Fig. 4b) the maximum power is seen at frequencies 5×10^{-4}–1.5×10^{-3} Hz (10–30 min). The powers at lower frequencies are greatly reduced as compared to those in the convective region. The upper frequency cutoff seems to be determined by the buoyancy frequency: the buoyancy frequency, which is defined by the inverse of the buoyancy period without including the 2π factor, increases with height from $\sim$1.2 $\times$ 10^{-3} Hz (period $\sim$ 14 min) at 10 km altitude to $\sim$1.7 $\times$ 10^{-3} Hz ($\sim$10 min) at 100 km. It is noteworthy that short-period waves having frequencies near the buoyancy frequency are preferentially generated. At higher altitudes (Fig. 4a) a significant leakage of the power to frequencies higher than the buoyancy frequency is seen probably due to the contribution of turbulent eddies generated via the nonlinearity of primary waves.

The spectra at 60 km altitude in the weaker forcing cases (UNI-10% and UNI-1%) are shown in Fig. 5. The dominant modes are distributed over wavenumbers slightly higher than those in UNI-ST probably because the cell sizes in the weaker forcing cases are smaller. The frequency where the power is maximized is $\sim$30% lower in 10% heating case (UNI-10%) and $\sim$60% lower in 1% heating case (UNI-1%). This is attributed to the difference in the convective overturning time in the boundary layer (the convective cell height divided by the root-mean-square vertical velocity), which is
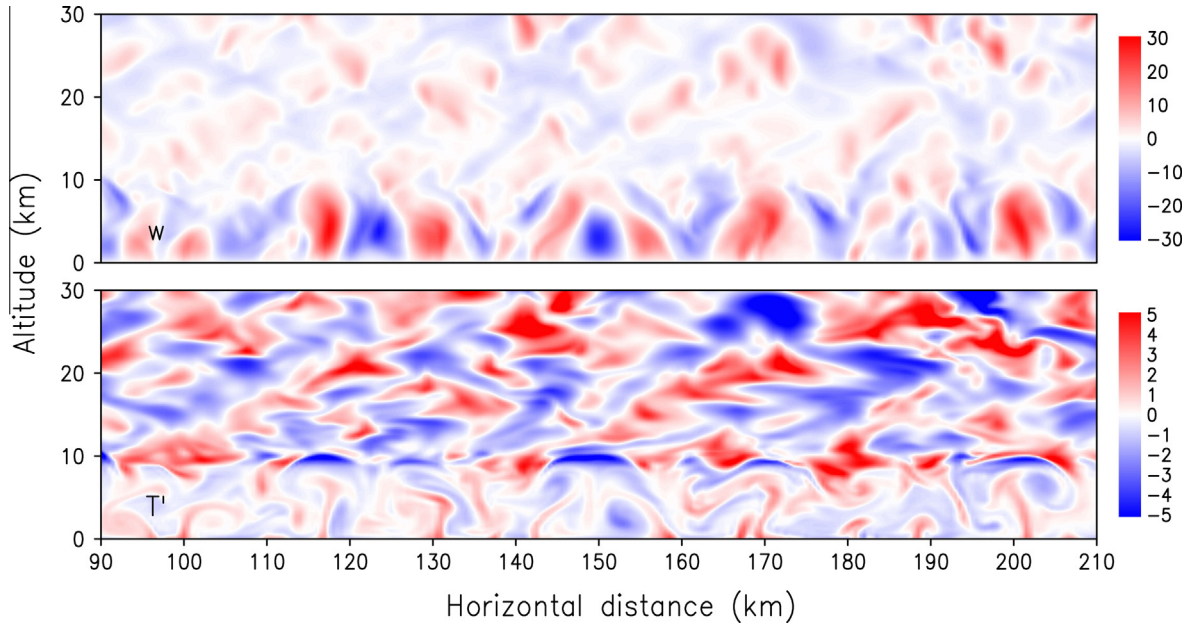
Fig. 2. Distributions of (upper) the vertical velocity in unit of m s^{-1} and (lower) the temperature perturbation in unit of K at 200 min in the standard forcing case of the uniform heating model (UNI-ST). A region near the surface is zoomed.
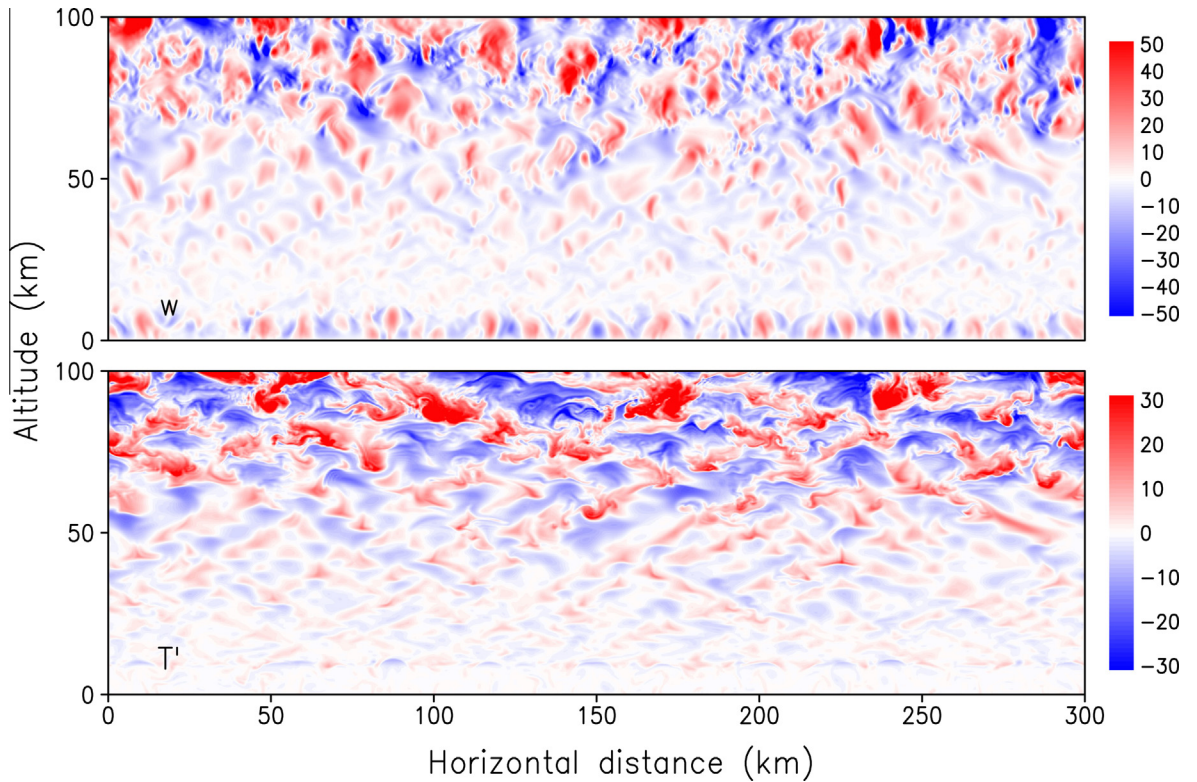

Fig. 3. Same as Fig. 2, but for the whole physical domain. Note that the scale bars differ from those in Fig. 2.

∼13 min in UNI-ST, ∼24 min in UNI-10%, and ∼50 min in UNI-1%. The amplitude is 10 times smaller in UNI-10% and 1000 times smaller in UNI-1% than in UNI-ST.

3.2. Localized heating

In the localized heating model, an upward motion of a plume is initiated near the surface around the center of the horizontal domain, and the penetration of the plume into the overlying stable layer generates gravity waves. The plume develops into smaller convection cells with time, and these cells also generate gravity waves; a snapshot near the source region is shown in Fig. 6. In the standard heating case (LOC-ST), the vertical velocity in the convection reaches 10–20 m s^{-1}, being similar to the modeling of a local dust storm by Spiga et al. (2013). In LOC-ST and 30 km-span heating case (LOC-30 km) the amplitudes of gravity
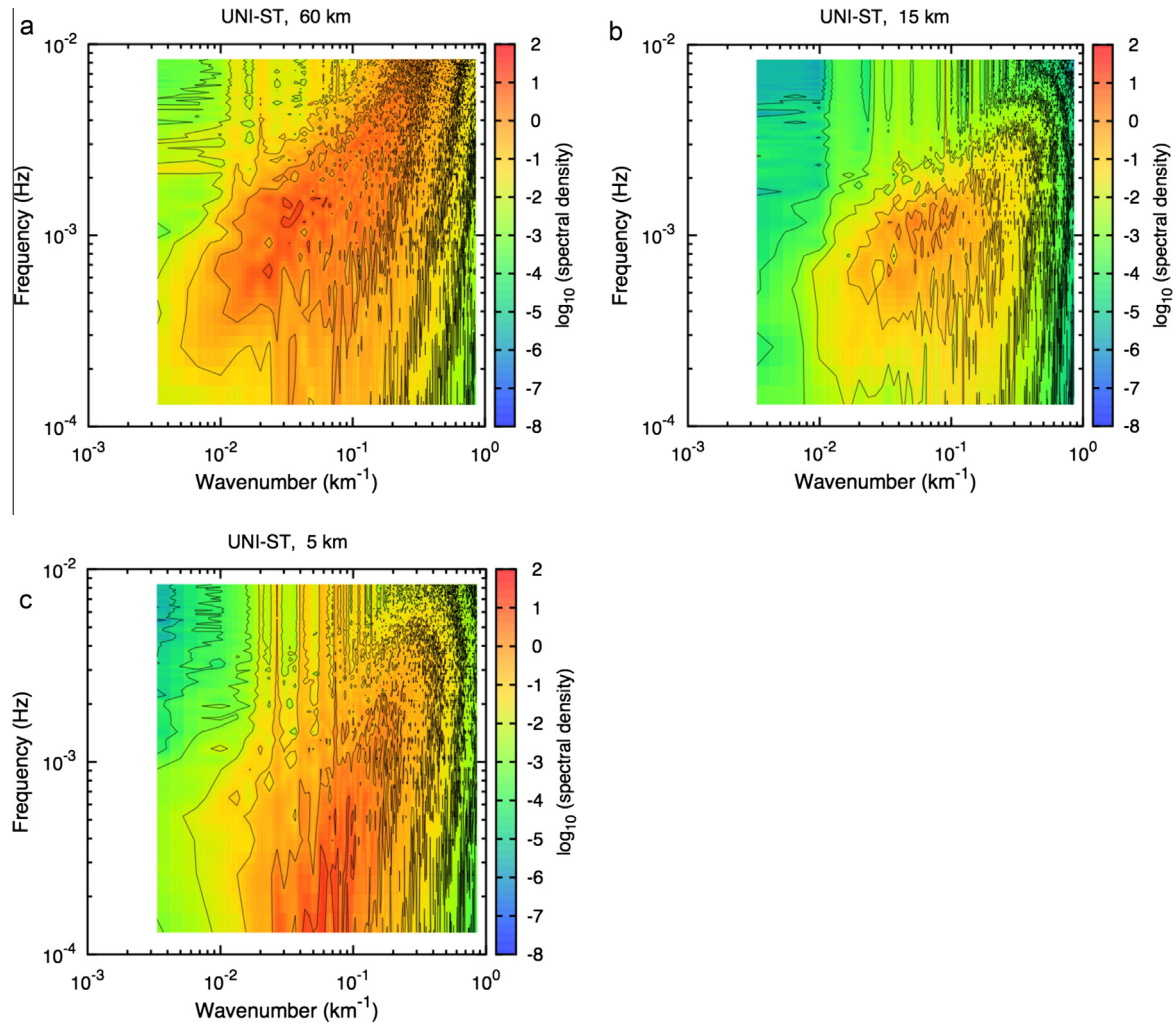
Fig. 4. Two-dimensional power spectra of the vertical velocity in the uniform heating model. (a) At 60 km, (b) 15 km and (c) 5 km altitude in the standard heating case (UNI-ST). The unit of the spectral density is $m^2\,s^{-2}/\log_2(wavenumber)/\log_2(frequency)$. The time interval for computing the spectrum is 200–328 min.
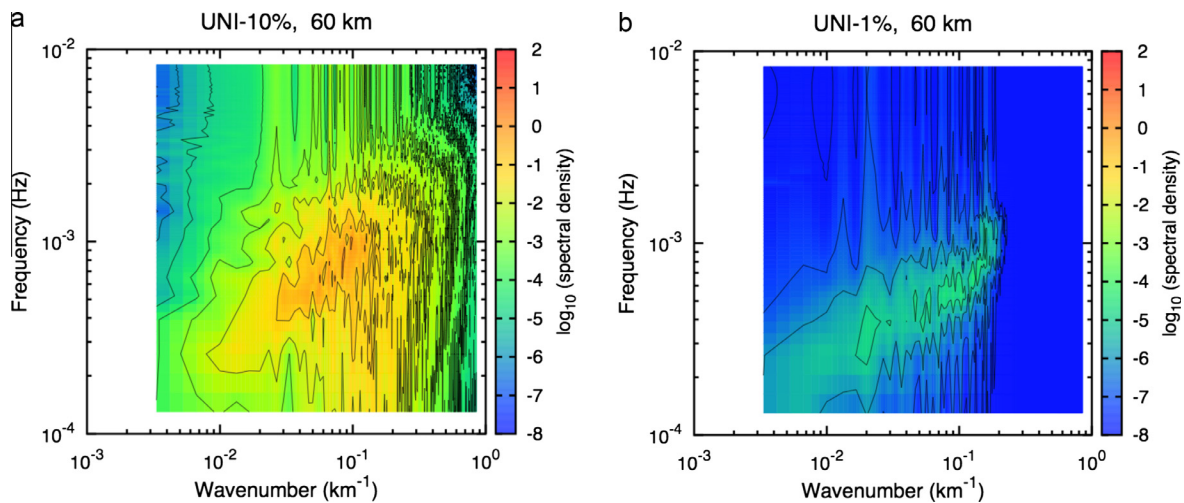

Fig. 5. Same as Fig. 4, but for (a) 60 km altitude in 10% heating case (UNI-10%) and (b) 60 km altitude in 1% heating case (UNI-1%). The time interval for computing the spectra is 360–488 min.

waves above 50 km reach maxima around the time of 180 min, while in the weaker forcing case (LOC-10%) they reach maxima around ~400 min. The wave field in LOC-ST in the whole domain at 180 min is shown in Fig. 7. The inclination of the phase surfaces is 30–45°, suggesting short-period waves. The amplitudes of the gravity waves grow with height and induce convective overturning above ~70 km.
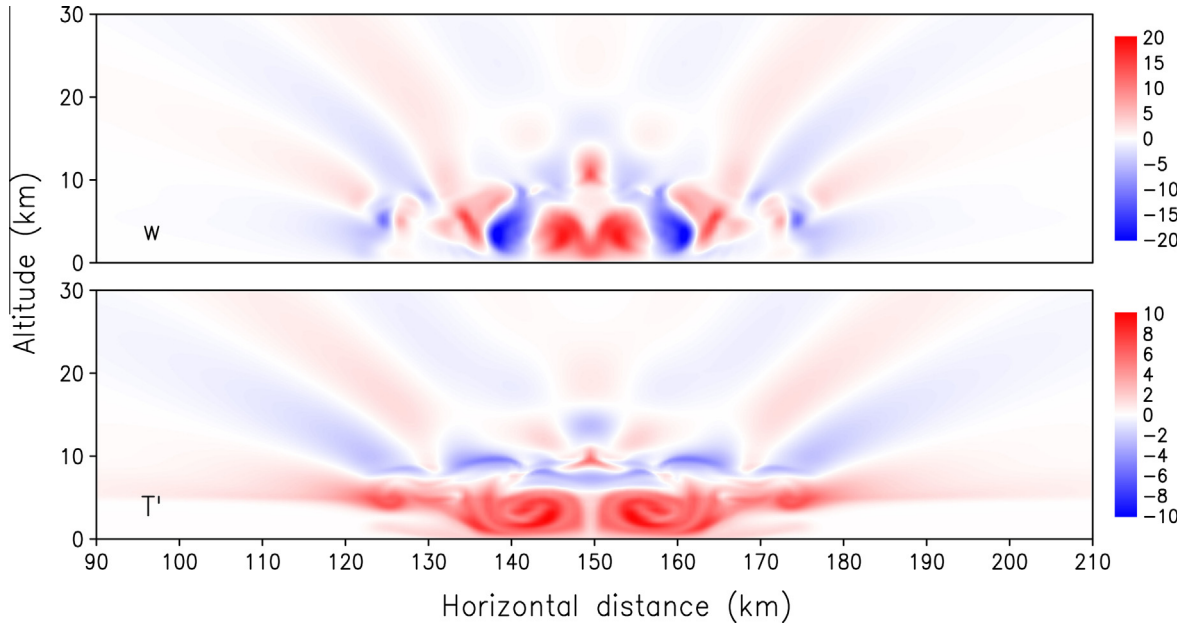
Fig. 6. The distributions of (upper) the vertical velocity in unit of m s^{-1} and (lower) the temperature perturbation in unit of K at 90 min in the standard forcing case of the local heating model (LOC-ST). A region near the source region is zoomed.

Fig. 8 shows the two-dimensional power spectra of the vertical velocity at 60 km altitude in the standard heating case (LOC-ST), 10% heating case (LOC-10%), and 30 km-span heating case (LOC-30 km). The dominant frequencies and wavenumbers are similar to those in the uniform heating model (Section 3.1): short-period waves having frequencies near the buoyancy frequency are preferentially generated, and the dominant horizontal wavelength is 10–50 km, being consistent with the horizontal scale of the convection cells. A leakage of the power to frequencies higher than the buoyancy frequency due to turbulent eddies is seen similarly to the uniform heating model. The change of the horizontal span of the heating from 60 km (LOC-ST) to 30 km (LOC-30 km) shifts the dominant modes to higher wavenumbers by ∼30%. The frequency at which the power peaks is 8×10^{-4}–2×10^{-3} Hz (periods of 8–20 min) in LOC-ST and LOC-30 km, while it is ∼30% less in the weak forcing case (LOC-10%). The amplitude is 10 times smaller in LOC-10% than in LOC-ST.

3.3. Comparison with observations

In both the uniform heating model and the localized heating model, the power of gravity waves is distributed mostly in the horizontal wavelength range of 10–100 km. The result is consistent with the MGS and Mars Odyssey's accelerometer observations showing the dominance of waves with horizontal scales of 20–200 km (Withers, 2006; Creasey et al., 2006b; Fritts et al., 2006) and the Mars Express airglow observations showing the horizontal scales of 50–150 km (Altieri et al., 2012). It is possible that inclusion of radiatively active dust in the localized heating model leads to generation of waves with longer horizontal wavelengths, because upward plumes are continuously powered by solar heating (Spiga et al., 2013), thereby increasing the size of convective motions. This effect may explain the slightly larger scales in the observations than in the model.

The vertical wavelengths are typically 10–20 km below 50 km altitude and longer at higher altitudes. The vertical structures of such long-vertical wavelength waves are only marginally observed by limb sounding methods such as radio occultation, because only short-vertical wavelength (typically <15 km) waves are identified

by applying high-pass filtering to temperature profiles. Nevertheless, observations suggest temperature amplitudes of 3–5 K for vertical wavelengths of 10–15 km below 40 km altitude (Creasey et al., 2006a; Ando et al., 2012), which are comparable to the model results.

4. Linear wave solutions

4.1. Model description

To study the propagation and dissipation processes of specific waves seen in the convection model, we solve the vertical structures using a full-wave model (e.g., Schubert et al., 2003). The model solves the linearized equations of continuity, momentum, and energy for a compressible, viscous, and thermally conducting atmosphere. The linearized equations used are summarized in the Appendix of Schubert et al. (2003). The grid interval is 1 km. The model physical domain extends from 0 km to 500 km, and below the physical domain a Rayleigh damping layer exists at altitudes from −200 km to 0 km. A Rayleigh damping layer is not needed for the upper boundary because molecular viscosity strongly attenuates waves and prevents wave reflection. Considering that the exobase is located at 200–250 km altitudes depending on the solar EUV condition, solutions of the fluid dynamical model above ∼250 km have no physical significance. The background temperature profile is shown in Fig. 1, and the background atmosphere is assumed to be at rest.

Waves are forced by a periodic heating in a 4 km-thick, Gaussian-shaped layer centered at 5 km altitude. The wave amplitude is scaled so that the wave is marginally saturated at high altitudes, i.e., the maximum amplitude of the horizontal velocity in the model domain is equal to the horizontal phase velocity. Since the dominant wave modes seen in the convection model have amplitudes large enough for breaking at high altitudes, giving marginally-saturated amplitudes enables evaluation of the wave characteristics in the region where molecular dissipation is dominant over saturation. The wave amplitude in the convection model was evaluated at the height of 60 km, which exceeds the vertical wavelengths of the waves studied.
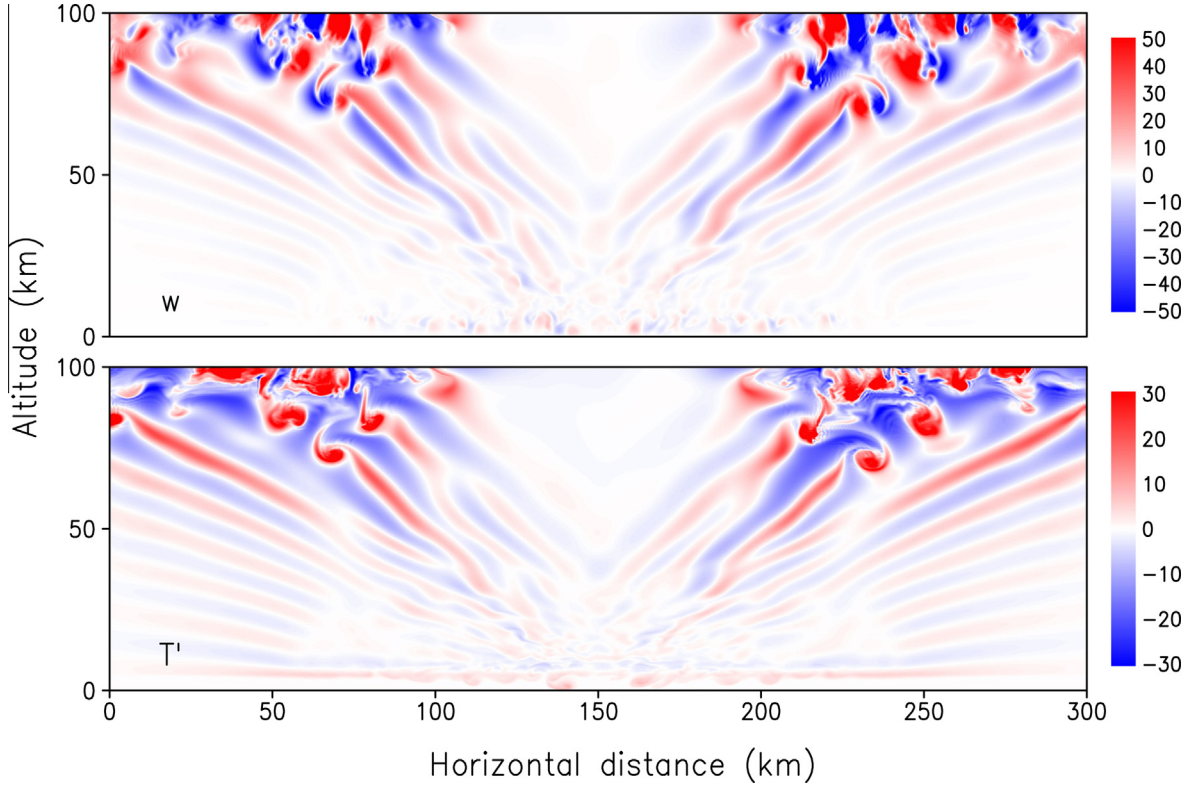
Fig. 7. Same as Fig. 6, but for the whole physical domain at 180 min. Note that the scale bars differ from those in Fig. 6.

Molecular viscosity and conduction become important for damping gravity waves at high altitudes. We use the coefficient of molecular viscosity μ_{CO_2} and the coefficient of molecular thermal conduction λ_{CO_2} of CO_2 that were obtained by Chapman and Cowling (1970) and used in the Mars GCM by Takahashi et al. (2003):

$$\mu_{CO_2} = 1.38 \times 10^5 \cdot \left(\frac{T}{273}\right)^{0.933} \qquad (8)$$

$$\lambda_{CO_2} = 1.64\, c_v\, \mu_{CO_2}, \qquad (9)$$

where c_v is the specific heat at constant volume. Since molecular diffusion coefficient for momentum and heat are given by μ_{CO_2}/ρ and $\lambda_{CO_2}/c_v\rho$, respectively, the effect of molecular dissipation increases exponentially with height.

Radiative damping can have non-negligible influence on gravity waves in the martian upper atmosphere (Imamura and Ogawa, 1995; Eckermann et al., 2011). According to the model calculation by Eckermann et al. (2011), the radiative damping rate is not sensitive to the vertical wavelength in the wavelength range 20–50 km. The damping rates for such long-vertical wavelength waves given in their paper are well represented as a function of the altitude, in unit of day^{-1}, by

$$\tau^{-1} = 12 \exp\left(-\frac{(z-120)^2}{15^2}\right) + 10 \exp\left(-\frac{(z-120)^2}{40^2}\right), \qquad (10)$$

where the altitude z is given in kilometers. The results presented in this section would be largely unchanged by the wavelength dependence neglected here, because the reduction of the wave amplitude by radiative damping is not larger than ~10%.

Eddy diffusion is not included in the model because its magnitude is highly uncertain and the effect is considered to be minor. The waves studied here have vertical wavelengths of >10 km and

periods of <30 min. Assuming a modest diffusion coefficient of <100 $m^2\,s^{-1}$ and a vertical wavelength of >10 km, the diffusion time scale is calculated to be $(10\,km/2\pi)^2/(100\,m^2\,s^{-1}) \sim 7\,h$ or longer. Such a slow process does not influence the short-period waves under study.

Based on the obtained wave field, we calculate the heating rate Q by (Schubert et al., 2003)

$$\bar{\rho} c_p Q = \langle \sigma' : \nabla \mathbf{v}' \rangle - \frac{d}{dz}(c_p \bar{\rho} \langle w' T' \rangle) + \langle \mathbf{v}' \cdot \nabla p' \rangle - \frac{d\bar{p}}{dz} \frac{\langle w' \rho' \rangle}{\bar{\rho}}, \qquad (11)$$

where $\bar{\rho}$ is the background density, c_p is the specific heat at constant pressure, the angle brackets denote horizontal and temporal average, σ' is the molecular viscous stress tensor of the wave field, $\mathbf{v}'$ is the wave velocity vector, w' is the wave vertical velocity, T' is the wave temperature perturbation, p' is the wave pressure perturbation, and ρ' is the wave density perturbation. The first term on the right hand side is the heating rate due to viscous dissipation of wave kinetic energy, the second term is the sensible heat flux divergence, the third term is the work done by the wave-induced pressure gradients, and the fourth term is the work done by the second-order wave-induced Eulerian drift in transporting mass in the gravitational field.

In the absence of the background wind as assumed in the present model, waves propagating in opposite directions exist with equal strength, and thus the net transport of horizontal momentum is zero. However, in the real martian atmosphere, a non-zero background wind filters out gravity waves traveling in the same direction and favors the vertical propagation of others. The momentum deposition by the waves reaching high altitudes is considered to play important roles in the momentum balance and the formation of the meridional circulation (Barnes, 1990; Kuroda et al., 2009; Medvedev et al., 2011a, 2011b). Considering
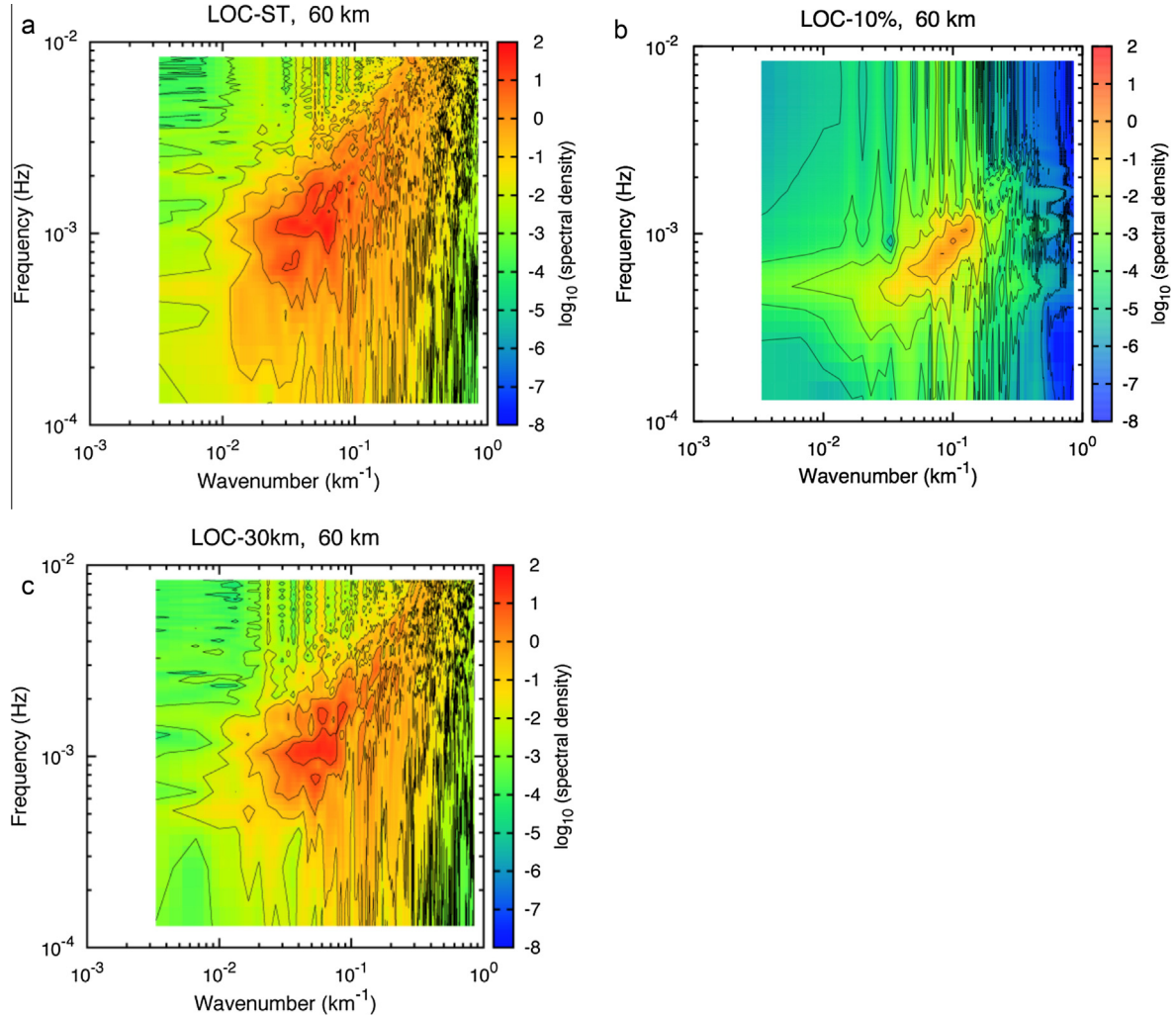
Fig. 8. Two-dimensional power spectra of the vertical velocity at 60 km altitude in the localized heating model. (a) Standard heating case (LOC-ST), (b) 10% heating case (LOC-10%), and (c) 30 km-span heating case (LOC-30 km). The unit of the spectral density is $m^2\ s^{-2}/log_2$(wavenumber)$/log_2$(frequency). The time interval for computing the spectra is 120–248 min for LOC-ST and LOC-30 km, and 360–488 min for LOC-10%.

such a potential importance in momentum transport, we calculate the acceleration caused by each dissipating wave by

$$\text{acceleration} = -\frac{1}{\bar{\rho}}\frac{d}{dz}\bar{\rho}\langle u'w' \rangle, \qquad (12)$$

where u' is the wave horizontal velocity.

We also examine how wave-induced turbulent mixing can influence the height of the homopause, although large-scale dynamics is considered to play crucial roles in controlling it (González-Galindo et al., 2009). Lindzen (1981) considered gravity waves saturated via convective instability and suggested that the turbulent diffusion coefficient induced by such waves is given by

$$K = \gamma \frac{kc^4}{2HN^3}, \qquad (13)$$

where k is the horizontal wavenumber, c is the horizontal phase velocity, H is the scale height, and N is the buoyancy frequency. The efficiency parameter γ, which was not included in Lindzen's (1981) original formulation, accounts for the spatially and temporally localized character of turbulence. Although the appropriate value of γ is not known, previous modeling studies adopted $\gamma = 0.2$ (Barnes, 1990; Théodore et al., 1993; Joshi et al., 1995). Here we further consider the uneven distribution with respect to the lat-

itude and the local time, and tentatively adopt $\gamma = 0.1$. The molecular diffusion coefficient is calculated for N_2 in a CO_2 atmosphere using the formula $D = 1.2 \times 10^{20}/n$ in unit of $m^2\ s^{-1}$, where n is the number density in m^{-3} (Leovy, 1982). Then, finding the altitude where $K = D$, we obtain the homopause height determined by wave-induced turbulence (Leovy, 1982; Yamanaka, 1995).

4.2. Linear solutions

Among the dominant modes seen in the standard heating case of the uniform heating model (UNI-ST) shown in Fig. 4, we adopt the horizontal wavelength of 50 km and the periods of 15 and 30 min. The obtained vertical structures are shown in Figs. 9 and 10. The amplitudes of these modes seen in the convection model are 4–10 times larger than those required for breaking at high altitudes, validating the linear solutions with marginally-saturated amplitudes. The vertical wavelengths of the 15 and 30-min waves are 50 km and 20 km, respectively. Because of the long wavelengths and the resultant fast vertical propagation, the wave amplitudes grow with height up to 120–150 km altitudes, above which the waves decay due to molecular viscosity and conductivity. The maximum amplitude of the fractional density is as large as 16% for the 15-min wave and 9% for the 30-min wave, which are comparable to the amplitudes of 5–50% observed in the lower ther-
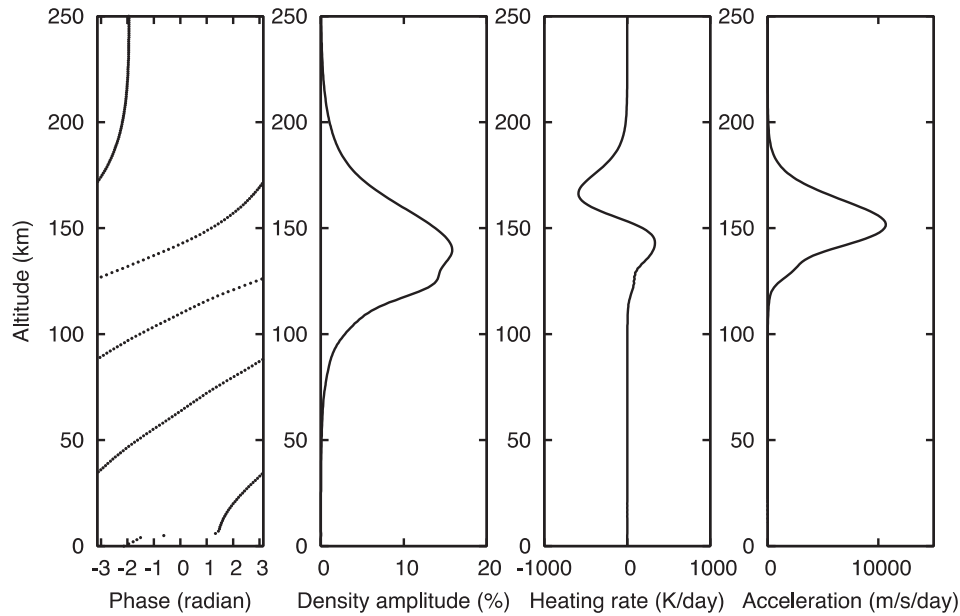
Fig. 9. Vertical structure of a gravity wave with a horizontal wavelength of 50 km and a period of 15 min. The wave-induced homopause is located at 137 km.
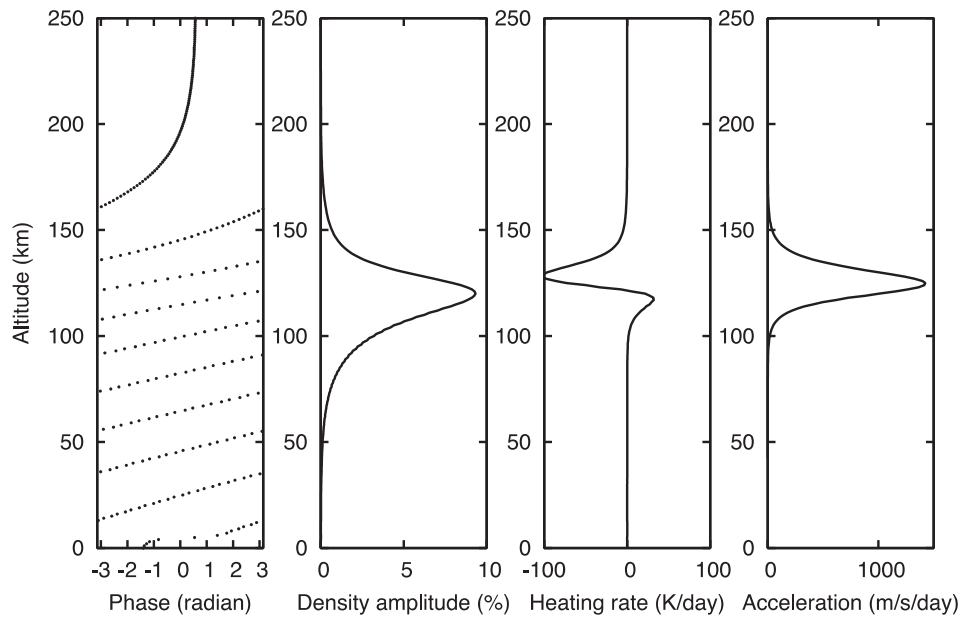

Fig. 10. Vertical structure of a gravity wave with a horizontal wavelength of 50 km and a period of 30 min. The wave-induced homopause is located at 112 km.

mosphere by accelerometers during aerobraking (Withers, 2006; Creasey et al., 2006b; Fritts et al., 2006). Both heating and cooling occur depending on the altitude, being consistent with previous linear models (Parish et al., 2009); the estimated values of 100 K d^{-1} or more are comparable to the contribution of radiative heating and cooling in the lower thermosphere (Medvedev and Yiğit, 2012). The estimated wave-induced accelerations of 1000–10,000 m s^{-1} day^{-1} are similar to those seen in a martian GCM (Medvedev et al., 2011a, 2011b). The wave-induced homopause is located at 137 km altitude for the 15-min wave; this altitude is comparable to 120–130 km estimated from direct measurements (Nier and McElroy, 1977).

In addition to the dominant wave modes seen in the convection model, Fig. 11 shows the solution of a wave having a longer horizontal wavelength of 100 km and a period of 15 min. Because of

the long vertical wavelength and the fast vertical propagation, the wave retains large amplitudes at altitudes as high as 250 km; the amplitude of the fractional density is around 10% at 120–220 km altitudes. The significant heating with a peak value of 700 K day^{-1} at ~170 km altitude may mitigate or cancel out the wave-induced cooling caused by slower waves. We should note, however, that the amplitude of this wave mode seen in the convection model (UNI-ST) is close to the amplitude that marginally causes breaking, and thus there is a large uncertainty on the modeled amplitude and the occurrence of wave-induced turbulence.

In 10% heating case (UNI-10%) shown in Fig. 5a, dominant modes are distributed over lower frequencies and/or higher wavenumbers. The solution of a wave with a horizontal wavelength of 20 km and a period of 30 min, around which the power is maximized, is shown in Fig. 12. The grid interval is 0.25 km only
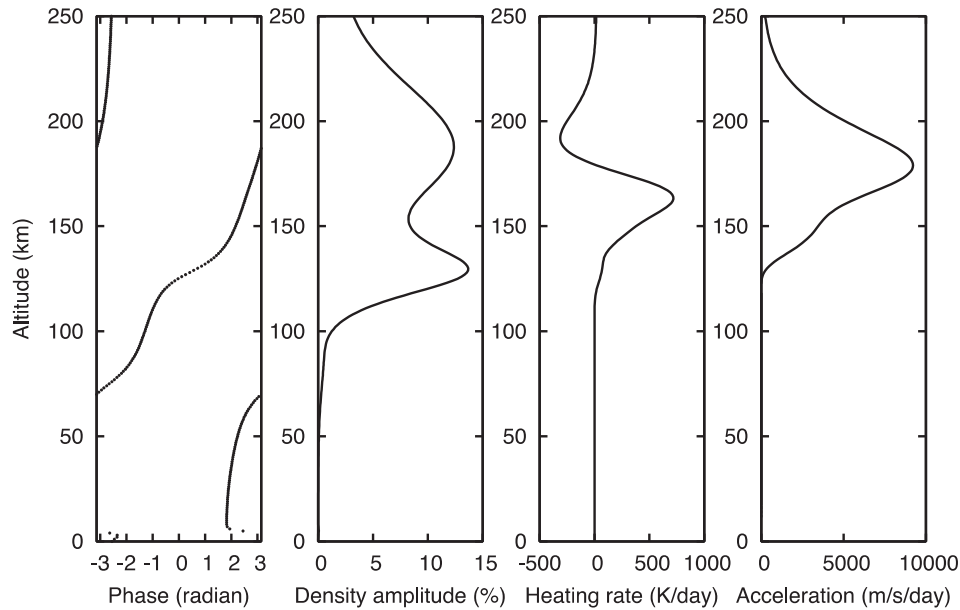
Fig. 11. Vertical structure of a gravity wave with a horizontal wavelength of 100 km and a period of 15 min. The wave-induced homopause is located at 173 km.

in this calculation. The vertical wavelength is as short as ~10 km, and the wave is strongly damped above ~100 km altitude because of the slow vertical propagation. The amplitude of this mode seen in UNI-10% is close to the amplitude that marginally causes breaking at high altitudes. In 1% heating case (UNI-1%) shown in Fig. 5b, the amplitudes of the dominant modes are even smaller and the waves do not cause breaking.

The result of the localized heating model (Fig. 8) shows similar characteristics for the dominant modes. Considering the inherent overestimation of the amplitude in the two-dimensional model (Section 2.3) and the episodic nature of local dust storms, the contribution in the real atmosphere would be much less, although the superposition of waves from different sources might increase the contribution depending on their spatial distribution.

5. Summary and conclusions

The properties of gravity waves generated by convection on Mars were studied using a nonlinear, two-dimensional, local model. Two types of forcing functions were tested: a horizontally-uniform heating for driving a boundary-layer convection, and a localized heating for driving a plume representing a local dust storm. In both of the experiments the dominant horizontal wavelengths of the generated gravity waves are 10–50 km, reflecting the spatial scale of convection cells, and non-negligible amplitudes are seen up to a wavelength of ~100 km. This result is consistent with the MGS and Mars Odyssey's accelerometer observations showing the dominance of waves with horizontal scales of 20–200 km (Withers, 2006; Creasey et al., 2006b; Fritts et al., 2006) and the Mars Express airglow observations showing the horizontal scales of 50–150 km (Altieri et al., 2012). The dominant period occurs around 10–30 min, being close to the buoyancy period of 10–14 min. Generation of such short-period waves is attributed to the vigorous, fast convection due to the tenuous atmosphere. In weaker forcing cases with heating rates of 10% and 1% of the standard value, the periods of the maximum power are longer due to slower convection, and the amplitudes are much less.

Though we modeled daytime convection only, convective wave generation might not be limited to the daytime. Hinson et al. (2014) analyzed radio occultation temperature profiles taken by

Mars Reconnaissance Orbiter and showed that detached neutral stability layers with several kilometers depth frequently occur during the nighttime probably due to convection that is driven from above by radiative cooling associated with the formation of water ice clouds. Although the convective heat fluxes in those detached neutral layers are unclear, we expect convective generation of gravity waves occurs also in the nighttime. The energy flux of the blackbody radiation from a 200 K surface is ~90 W m^{-2}, which is much larger than the heat flux in the present convection model. Numerical modeling of the nocturnal convection is left for future studies.

The vertical propagation of the dominant waves into the lower thermosphere was studied using a linear wave model. The amplitudes of the waves are large enough for saturation (breaking) at high altitudes, and thus the suggested amplitude, heating rate and acceleration above the breaking height are considered to be insensitive to the source strength. The vertical wavelengths are as long as 20–50 km, and the waves retain large amplitudes up to 150–200 km altitudes because of the fast vertical propagation. The calculated amplitudes in the fractional density of up to 16% in the lower thermosphere are comparable to the amplitudes of 5–50% observed by MGS and Mars Odyssey's accelerometers (Withers, 2006; Creasey et al., 2006b; Fritts et al., 2006). The magnitudes of the heating and cooling caused by the dissipation of the waves are comparable to the contribution of radiation, and the wave-induced acceleration can play significant roles in the formation of the planetary-scale circulation. The altitude of the wave-induced homopause is roughly consistent with the observed homopause height, suggesting that wave-induced turbulent mixing as well as large-scale circulation is important. Considering that both the wavelength and the period are determined by the simple fluid dynamics of convection, and that the amplitude is mostly determined by saturation, the conclusions drawn from the current two-dimensional model are expected to be robust, although three-dimensional modeling with a realistic background is needed to test the predictions.

Medvedev and Yiğit (2012) and Medvedev et al. (2015) suggested, based on Mars GCMs with a gravity wave parameterization, that wave-induced cooling exceeds wave-induced heating in the lower thermosphere (>110 km) and that the cooling might explain the discrepancy between the observed and
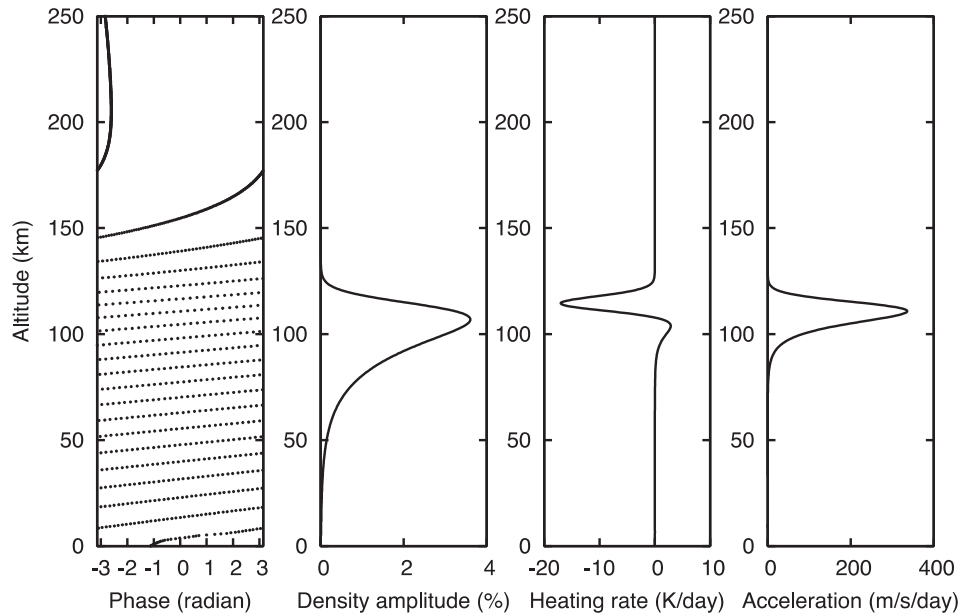
Fig. 12. Vertical structure of a gravity wave with a horizontal wavelength of 20 km and a period of 30 min. The wave-induced homopause is located at 95 km.

model-derived temperatures. In their gravity wave scheme a Gaussian-shaped phase velocity spectrum is assumed for the source of gravity waves; the dispersion (half width at e^{-1} decay) of the horizontal phase velocity is 35 m s^{-1} and the prescribed horizontal wavelength is 200 km, implying that the typical period is 95 min. However, given the results of the present study, much shorter-period waves can be dominant depending on the illumination condition, and such waves might propagate to higher altitudes and cause net heating up to the altitudes of 150–180 km. For better constraining the wave characteristics and its variability, experiments with a broad range of forcing parameters and background states are needed.

Observations by NASA's MAVEN provide opportunities for constraining the wave characteristics: the MAVEN's neutral and ion measurements (Mahaffy et al., 2014) detected substantial wavelike structures in the densities of various neutral and ion species in the lower thermosphere (Mahaffy et al., 2015). Observations of the geographical and temporal variations of the wave activity would reveal their sources and propagation characteristics. Observations of the seasonal variation of the homopause would also constrain the importance of gravity waves in the vertical mixing of the thermosphere. The martian GCM by González-Galindo et al. (2009), which extends to the thermosphere and does not include wave-induced turbulence, predicts seasonal variation of the homopause with higher homopause altitudes in the solstices than in the equinoxes in all latitude regions due to a reinforced general circulation in the solstices. The contribution of gravity waves should have different seasonal and latitudinal tendencies depending on the wave sources.

The results obtained in this study have an important implication for the early martian atmosphere, which could have been much thicker than today with the surface pressure of ∼2 bar (Chassefière et al., 2007). The denser atmosphere means a weaker heating rate, which should lead to the lowering of the dominant frequency of convectively-generated waves, and then the lowering of the wave's penetration height. The amplitudes of the waves should also be reduced. Accordingly the wave-induced turbulence and the wave-driven large-scale circulation in the thermosphere would be attenuated, leading to the lowering of the homopause height. Large-scale waves such as thermal tides have been considered to be essential as well in driving the martian thermospheric

circulation (González-Galindo et al., 2009); the reduction of the heating rate in the lower atmosphere would also reduce the contributions of such large-scale waves. A similar argument is possible for topographically-generated waves, because a thicker atmosphere favors weaker jets near the surface (Forget et al., 2013). The homopause height has a large influence on the thermospheric composition. Assuming that the major species with a molecular mass m_0 and a minor species with a molecular mass m_1 are independently in diffusive equilibrium in the heterosphere and they are well mixed in the homosphere, the mole fraction of the minor species would be multiplied by e (∼2.72) when the homopause is lowered by $\Delta z = H_0/(1 - m_1/m_0)$, where H_0 is the scale height of the major species. Letting the major species be CO_2 and the minor species be H_2, and assuming an atmospheric temperature of 200 K, we have $\Delta z \sim 11$ km. Based on the comparison of the wave's penetration height between the wave modes seen in the standard heating case and 10% heating case (Figs. 9 and 12), the homopause on early Mars could have been at least 40 km lower, leading to an increase of the mole fraction of H_2 by a factor of 30 or more. Since the escaping fluxes of minor species depend on their thermospheric densities, a lower homopause may have enhanced the escape of light, minor species to space.

Acknowledgments

References

Altieri, F. et al., 2012. Gravity waves mapped by the OMEGA/MEX instrument through O$_2$ dayglow at 1.27 μm: Data analysis and atmospheric modeling. J. Geophys. Res. 117, E00J08. http://dx.doi.org/10.1029/2012JE004065.

Ando, H., Imamura, T., Tsuda, T., 2012. Vertical wavenumber spectra of gravity waves in the martian atmosphere obtained from Mars Global Surveyor radio occultation data. J. Atmos. Sci. 69, 2906–2912. http://dx.doi.org/10.1175/JAS-D-11-0339.1.

Barnes, J.R., 1990. Possible effects of breaking gravity waves on the circulation of the middle atmosphere of Mars. J. Geophys. Res. 95, 1401–1421.

Chapman, S., Cowling, T.G., 1970. The Mathematical Theory of Non-uniform Gasses. Cambridge Univ. Press, New York, 423pp.

Chassefière, E., Leblanc, F., Langlais, B., 2007. The combined effects of escape and magnetic field histories at Mars. Planet. Space Sci. 55, 343–357.

Creasey, J.E., Forbes, J.M., Hinson, D.P., 2006a. Global and seasonal distribution of gravity wave activity in Mars' lower atmosphere derived from MGS radio occultation data. Geophys. Res. Lett. 33, L01803. http://dx.doi.org/10.1029/2005GL024037.

Creasey, J.E., Forbes, J.M., Keating, G.M., 2006b. Density variability at scales typical of gravity waves observed in Mars' thermosphere by the MGS accelerometer. Geophys. Res. Lett. 33, L22814. http://dx.doi.org/10.1029/2006GL027583.

Eckermann, S.D., Ma, J., Zhu, X., 2011. Scale-dependent infrared radiative damping rates on Mars and their role in the deposition of gravity-wave momentum flux. Icarus 211, 429–442.

Forget, F. et al., 2013. 3D modelling of the early martian climate under a denser CO_2 atmosphere: Temperatures and CO_2 ice clouds. Icarus 222, 81–99.

Fovell, R., Durran, D., Holton, J.R., 1992. Numerical simulations of convectively generated stratospheric gravity waves. J. Atmos. Sci. 49, 1427–1442.

Fritts, D.C., Wang, L., Tolson, R.H., 2006. Mean and gravity wave structures and variability in the Mars upper atmosphere inferred from Mars Global Surveyor and Mars Odyssey aerobraking densities. J. Geophys. Res. 111, A12304. http://dx.doi.org/10.1029/2006JA011897.

González-Galindo, F. et al., 2009. A ground-to-exosphere martian general circulation model: 1. Seasonal, diurnal, and solar cycle variation of thermospheric temperatures. J. Geophys. Res. 114, E04001. http://dx.doi.org/10.1029/2008JE003246.

Goya, K., Miyahara, S., 1999. A non-hydrostatic and compressible 2-D model simulation of internal gravity waves generated by convection. Earth Planets Space 51, 485–498.

Haberle, R.M. et al., 1993. A boundary-layer model for Mars: Comparison with Viking lander and entry data. J. Atmos. Sci. 50, 1544–1559.

Heavens, N.G. et al., 2010. Convective instability in the martian middle atmosphere. Icarus 208, 574–589. http://dx.doi.org/10.1016/j.icarus.2010.03.023.

Hinson, D.P. et al., 1999. Initial results from radio occultation measurements with Mars Global Surveyor. J. Geophys. Res. 104, 26997–27012.

Hinson, D.P. et al., 2008. The depth of the convective boundary layer on Mars. Icarus 198, 57–66.

Hinson, D.P. et al., 2014. Initial results from radio occultation measurements with the Mars Reconnaissance Orbiter: A nocturnal mixed layer in the tropics and comparisons with polar profiles from the Mars Climate Sounder. Icarus 243, 91–103.

Horinouchi, T., Nakamura, T., Kosaka, J., 2002. Convectively generated mesoscale gravity waves simulated throughout the middle atmosphere. Geophys. Res. Lett. 29, 2007. http://dx.doi.org/10.1029/2002GL016069.

Imamura, T., Ogawa, T., 1995. Radiative damping of gravity waves in the terrestrial planetary atmospheres. Geophys. Res. Lett. 22, 267–270.

Imamura, T., Kawasaki, Y., Fukuhara, T., 2007. Mesoscale spectra of Mars's atmosphere derived from MGS TES infrared radiances. J. Atmos. Sci. 64, 1717–1726.

Imamura, T. et al., 2014. Inverse insolation dependence of Venus' cloud-level convection. Icarus 228, 181–188.

Joshi, M.M., Lawrence, B.N., Lewis, S.R., 1995. Gravity wave drag in three-dimensional atmospheric models of Mars. J. Geophys. Res. 100, 21235–21245.

Klemp, J.B., Wilhelmson, R.B., 1978. The simulation of three-dimensional convective storm dynamics. J. Geophys. Res. 35, 1070–1096.

Kuroda, T. et al., 2009. On forcing the winter polar warmings in the martian middle atmosphere during dust storms. J. Meteorol. Soc. Jpn. 87, 913–921. http://dx.doi.org/10.2151/jmsj.87.913.

Lane, T.P., Clark, T.L., 2002. Gravity waves generated by the dry convective boundary layer: Two-dimensional scale selection and boundary-layer feedback. Q. J. R. Meteorol. Soc. 128, 1543–1570.

Leovy, C.B., 1982. Control of the homopause level. Icarus 50, 311–321.

Lewis, S. et al., 1999. A climate database for Mars. J. Geophys. Res. 104, 24177–24194.

Lindzen, R.S., 1981. Turbulence and stress owing to gravity wave and tidal breakdown. J. Geophys. Res. 86, 9707–9714.

Magalhães, J.A., Schofield, J.T., Seiff, A., 1999. Results of the Mars Pathfinder atmospheric structure investigation. J. Geophys. Res. 104, 8943–8956.

Mahaffy, P.R. et al., 2014. The Neutral Gas and Ion Mass Spectrometer on the Mars atmosphere and volatile evolution mission. Space Sci. Rev. http://dx.doi.org/10.1007/s11214-014-0091-1 (Published online).

Mahaffy, P.R. et al., 2015. Early composition, structure, and isotope measurements in the upper atmosphere of Mars from MAVEN'S Neutral Gas and Ion Mass Spectrometer (NGIMS). Lunar Planet. Sci. 46. Abstract 1981 (The Woodlands, Texas, March 16–20).

Medvedev, A.S., Yiğit, E., 2012. Thermal effects of internal gravity waves in the martian upper atmosphere. J. Geophys. Res. 39, L05201. http://dx.doi.org/10.1029/2012GL050852.

Medvedev, A.S., Yiğit, E., Hartogh, P., 2011a. Estimates of gravity wave drag on Mars: Indication of a possible lower thermospheric wind reversal. Icarus 211, 909–912.

Medvedev, A.S. et al., 2011b. Influence of gravity waves on the martian atmosphere: General circulation modeling. J. Geophys. Res. 116, E10004. http://dx.doi.org/10.1029/2011JE003848.

Medvedev, A.S. et al., 2015. Cooling of the martian thermosphere by CO_2 radiation and gravity waves: An intercomparison study with two general circulation models. J. Geophys. Res. http://dx.doi.org/10.1002/2015JE004802 (Early View).

Michaels, T., Rafkin, S.C.R., 2004. Large-eddy simulation of atmospheric convection on Mars. Q. J. R. Meteorol. Soc. 130, 1251–1274. http://dx.doi.org/10.1256/qj.02.169.

Mueller-Wodarg, I.C.F. et al., 2008. Neutral atmospheres. Space Sci. Rev. 139, 191–234. http://dx.doi.org/10.1007/s11214-008-9404-6.

Nier, A.O., McElroy, M.B., 1977. Composition and structure of Mars' upper atmosphere: Results from the neutral mass spectrometers on Viking 1 and 2. J. Geophys. Res. 82, 4341–4349.

Odaka, M. et al., 1998. A numerical study of the martian atmospheric convection with a two-dimensional anelastic model. Earth Planets Space 50, 431–437.

Parish, H.F. et al., 2009. Propagation of tropospheric gravity waves into the upper atmosphere of Mars. Icarus 203, 28–37.

Pettengill, G.H., Ford, P.G., 2000. Winter clouds over the North martian polar cap. Geophys. Res. Lett. 27, 609–612.

Schubert, G., Hickey, M.P., Walterscheid, R.L., 2003. Heating of Jupiter's thermosphere by the dissipation of upward propagating acoustic waves. Icarus 163, 398–413.

Spiga, A. et al., 2012. Gravity waves, cold pockets and CO_2 clouds in the martian mesosphere. Geophys. Res. Lett. 39, L02201. http://dx.doi.org/10.1029/2011GL050343.

Spiga, A. et al., 2013. Rocket dust storms and detached dust layers in the martian atmosphere. J. Geophys. Res. 118, 746–767. http://dx.doi.org/10.1002/jgre.20046.

Takahashi, Y.O. et al., 2003. Topographically induced north–south asymmetry of the meridional circulation in the martian atmosphere. J. Geophys. Res. 108, 5018. http://dx.doi.org/10.1029/2001JE001638.

Théodore, B. et al., 1993. Solstitial temperature inversions in the martian middle atmosphere: Observational clues and 2-D modeling. Icarus 105, 512–528.

Tsuboki, K., Sakakibara, A., 2002. Large-scale parallel computing of Cloud Resolving Storm Simulator. In: Zima, H.P. et al. (Eds.), High Performance Computing. Springer, pp. 243–259.

Tsuboki, K., Sakakibara, A., 2007. Numerical prediction of high-impact weather systems. In: The Textbook for Seventeenth IHP Training Course, 281pp.

Walterscheid, R.L., Schubert, G., Brinkman, D.G., 2001. Small-scale gravity waves in the upper mesosphere and lower thermosphere generated by deep tropical convection. J. Geophys. Res. 106, 31825–31832.

Walterscheid, R.L., Hickey, M.P., Schubert, G., 2013. Wave heating and Jeans escape in the martian upper atmosphere. J. Geophys. Res. 118, 2413–2422. http://dx.doi.org/10.1002/jgre.20164.

Withers, P., 2006. Mars Global Surveyor and Mars Odyssey Accelerometer observations of the martian upper atmosphere during aerobraking. Geophys. Res. Lett. 33, L02201. http://dx.doi.org/10.1029/2005GL024447.

Wright, C.J., 2012. A one-year seasonal analysis of martian gravity waves using MCS data. Icarus 219, 274–282.

Yamanaka, M.D., 1995. Homopause control by gravity wave breaking in the planetary atmospheres. Adv. Space Res. 15 (4), 47–50.

Zurek, R.W., 1992. Comparative aspects of climate of Mars. In: Kieffer, H.H. et al. (Eds.), Mars. University of Arizona Press, Tucson, pp. 799–817.